



Atomically dispersed Fe-N-P-C complex electrocatalysts for superior oxygen reduction



Yahao Li^{a,1}, Bingxu Chen^{a,b,1}, Xuezhi Duan^b, Shuangming Chen^c, Daobin Liu^c, Ketao Zang^d, Rui Si^e, Fengliu Lou^a, Xuehang Wang^a, Magnus Rønning^a, Li Song^{c,*}, Jun Luo^{d,*}, De Chen^{a,*}

^a Department of Chemical Engineering, Norwegian University of Science and Technology, N-7491, Trondheim, Norway

^b State Key Laboratory of Chemical Engineering, East China University of Science and Technology, 130 Meilong Road, Shanghai, 200237, China

^c National Synchrotron Radiation Laboratory, CAS Center for Excellence in Nanoscience, University of Science and Technology of China, Hefei, Anhui, 230029, China

^d Center for Electron Microscopy and Tianjin Key Lab of Advanced Functional Porous Materials, Institute for New Energy Materials, School of Materials, Tianjin University of Technology, Tianjin, 300384, China

^e Shanghai Synchrotron Radiation Facility, Shanghai Institute of Applied Physics, Chinese Academy of Sciences, Shanghai, 201204, China

ARTICLE INFO

Keywords:

Atomically dispersed iron electrocatalyst
N,P co-doped carbon
Biomass
Oxygen reduction reaction
DFT calculations

ABSTRACT

Development of cost-effective electrocatalysts as an alternative to platinum for oxygen reduction reaction (ORR) is of great significance for boosting the applications of green energy devices such as fuel cells and metal-air batteries. Here we report a nitrogen and phosphorus tri-doped hierarchically porous carbon supported highly cost-effective, efficient and durable Fe single-site electrocatalyst derived from biomass. Combined aberration-corrected HAADF-STEM, XPS and XAFS measurements and theoretical calculations reveal the atomically dispersed Fe-N-P-C-O complex as the dominant active sites for ORR. This work also shows the design principle for enhancing the ORR activity of single Fe site catalysts with higher Fe charge, which can be manipulated by the coordinated structure in the active centre. Theoretical calculations reveal that the main effective sites are singleN-P-O-Fe-O centers, where the associated P-O-Fe bond can significantly lower the stability of strongly adsorbed O^{*} and OH^{*} on the catalytically active sites and thus give rise to enhanced ORR performance. The insights reported here open a new avenue for constructing highly efficient molecule-like heterogeneous catalysts in electrochemical energy technologies.

1. Introduction

Electrochemical reduction of oxygen, also known as oxygen reduction reaction (ORR), normally determines the efficiency of energy conversion and storage systems such as fuel cells and metal-air batteries, where the cost-effective catalysts are essential for their practical applications [1–5]. Complete oxygen reduction involves the transfer of four electrons with the cleavage of the O–O bond and the maximum release of energy [6,7]. Great efforts have been devoted to reduce the overpotential of ORR catalysts. One strategy is to increase the utilization efficiency of commonly used, highly active platinum-based ORR catalysts by increasing the proportion of Pt atoms exposed on the surface (i.e., the number of active sites) and/or enhancing the intrinsic activity of the active sites [8–11]. Another strategy is to develop alternative electrocatalysts such as metal-free [12–15] or precious-metal-free [16–20] materials with comparable or even better ORR

performance. Among them, nanocarbons have been demonstrated to be one of the most promising class of ORR catalysts, and their electrocatalytic performance can be further enhanced by introducing heteroatoms to modify the electronic and geometric structures [5,15,20–22]. In particular, Fe-N-C complex catalysts have been reported as possible replacement of Pt-based catalysts [20,22–24]. Thus, rational design of carbon-based ORR catalysts with low cost as well as high activity, selectivity and durability is of great significance.

For ORR in alkaline media, recent work [25,26] highlighted the significance of electronic structure of metal in oxide in controlling the competition between O₂²⁻/OH⁻ displacement and OH⁻ regeneration on metal ions as the rate-limiting steps of the ORR. Inspired by natural catalysts, such as cytochrome c oxidase [27], molecular catalysts, such as macrocyclic MN₄ metal complexes confined to electrode surfaces were also investigated and a ORR volcano plot between the ORR activity and M^{III}/M^{II} redox potential of MN₄ chelates or the M-O₂ binding

* Corresponding authors.

E-mail addresses: song2012@ustc.edu.cn (L. Song), jluo@tjut.edu.cn (J. Luo), chen@nt.ntnu.no (D. Chen).

¹ These authors contributed equally to this work.

energies [28] was established. Similar to heterogeneous catalysis, a proper adsorption strength of the reactant is required, which is typically governed by the electronic properties of metal ions in the active centre. However, efficiently tuning the electronic properties of the active sites to enhance the performance of ORR catalysts remains a challenge.

Herein, we report a simple and easy to scale-up impregnation-pyrolysis route to produce Fe, N and P tri-doped biomass derived porous carbon electrocatalyst (Fe-NPC) with unique atomically dispersed Fe-N-P-C complex active sites. The as-prepared cost-effective catalyst exhibited good ORR activity, long-term cycling stability and methanol tolerance in alkaline electrolyte, and outperformed commercialized Pt/C catalysts. With the help of advanced characterization such as aberration corrected HAADF-STEM and XAFS as well as systematic DFT calculations, the molecule-like structure of the complex was revealed as an active centre, in which the associated Fe-O-P bond significantly lower the stability of strongly adsorbed O[•] and OH[•] on the catalytically active sites and thus facilitated the oxygen reduction.

2. Experimental

Iron, nitrogen and phosphorus tri-doped wood briquette (WB) derived porous carbon electrocatalyst (Fe-NPC) was produced by an impregnation-pyrolysis method. The Norwegian WB was purchased from local supermarket. The properties of WB are presented in the supporting information. Firstly, 6 g of WB was dispersed in 200 mL precursor solution, which contained 1.5 mol/L of H₃PO₄ and 0.025 mol/L of FeCl₃, and vigorously stirred for 30 min. The resulted suspension was filtered with a vacuum filtration set-up and the filter cake was transferred onto a plastic sheet to dry overnight at room temperature. The dried sample was then transferred into a fix-bed reactor, heated to 1000 °C with a heating rate of 5 °C/min and kept for 2 h under an NH₃ flow with a flow rate of 50 mL/min. After cooling to room temperature in an Ar flow, the obtained black powder was reflux in distilled water at 110 °C overnight to remove any soluble salts that may formed during synthesis. After wash and dry, the Fe-NPC powder was obtained. To compare with, carbonized WB (CWB) were produced by simply carbonized WB powders under an Ar flow at 1000 °C for 2 h.

To compare the effects of different possible active sites, Fe-NPC-L was produced with the same method, and the concentration of FeCl₃ in the precursor solution was controlled to be 0.25 mmol/L. N and P co-doped WB derived carbon electrocatalyst (NPC) was produced also using the impregnation-calcination method, where 1.5 mol/L of H₃PO₄ solution was used as the precursor solution. Fe_xP/C composite was prepared with sodium alginate (SA), FeCl₃ and H₃PO₄ as the precursors for C, Fe and P, respectively. SA was firstly dissolved in distilled water to form a 15 wt% gel-like solution. 50 g of this solution was added drop wise into 200 mL solution containing 0.1 mol/L of FeCl₃ and H₃PO₄. As the SA coordinated with Fe³⁺, each drop solidified into a hollow particle. These particles were kept steady in the solution overnight and then dried at 80 °C for 12 h. As-obtained particles were transferred into a fix-bed reactor and heat treated under inert atmosphere at 800 °C for 1 h. After cooling to room temperature, the reactor was reheated to 1000 °C under NH₃ flow and kept for another 1 h. The powder obtained was also refluxed in distilled water overnight. Resulted materials is denoted as Fe_xP/C. Fe and N co-doped WB derived carbon (Fe-NC) was also produced with the impregnation-pyrolysis method, in which 0.25 mmol/L FeCl₃ alone was used as precursor solution. Fe and P co-doped WB derived carbon (Fe-PC) is produced using the same method as Fe-NPC but under Ar atmosphere.

Field emission scanning electron microscopy (FE-SEM, Q-200, Hillsboro, USA) was used to investigate the surface morphologies. Transmission electron microscopy (TEM) characterizations were conducted using a JEM-2100 F (JEOL Ltd, Japan) with an accelerating voltage of 200 kV. The high angle annular dark field (HAADF) scanning transmission electron microscopy (STEM) images and element mappings were taken using aberration corrected FEI Titan Cubed Themis G2

300 with an accelerating voltage of 200 kV. The N₂ sorption isotherms were performed on a Tristar II 3020 (Micromeritics Instruments, USA). Pore size distribution (PDS) was obtained from the isotherm results based on DFT calculation. A degassing step was applied to the catalysts at 200 °C for 12 h under turbo molecular vacuum pumping before the adsorption/desorption measurements. Temperature programmed oxidation (TPO) was carried out with a TG/DSC (STA449C, NETZSCH, USA). X-ray diffraction (XRD) of Fe-NPC was performed using a Bruker D8 Advance DaVinci X-ray diffractometer with Cu K α radiation ($\lambda = 1.54 \text{ \AA}$). X-ray fluorescence (XRF) was carried out using a Supermini 200 (Rigaku, Japan). X-ray photoelectron spectrometry (XPS) was performed using a Kratos XSAM 800 spectrometer (Manchester, UK) equipped with an Al K α X-ray (1486.6 eV, excitation source working at 15 kV). The C 1 s peak at 284.6 eV was taken as an internal standard to correct the shift in the binding energy caused by sample charging. Fe K-edge X-ray absorption fine structure (XAFS) spectra were acquired at beamline 14W1 in Shanghai Synchrotron Radiation Facility (SSRF), China, using Si (111) double-crystal monochromator in transmission mode. The storage ring of SSRF was operated at 3.5 GeV with the current of 300 mA. The energy position was calibrated with a Fe foil. The raw data were processed according to the standard procedures using the WinXAS3.1 program [29]. Theoretical amplitudes and phase-shift functions were calculated with the FEFF8.2 code [30]. X-ray absorption near edge structure (XANES) spectroscopy of N K-edge and P L_{2,3}-edge were performed at the MCD endstation at the beamline BL12B-a in the National Synchrotron Radiation Laboratory (NSRL), Hefei, China. The storage ring of the NSRL was operated at 0.8 GeV with a maximum current of 300 mA. The spectra were recorded at room temperature with an energy step of 0.2 eV and the total electron yield (TEY) detection mode.

The electrochemical oxygen reduction properties of as-obtained catalysts were evaluated with a three-electrode system at ambient condition using a Princeton VersaSTAT potentiostat analyzer (Princeton Applied Research). Both glassy carbon rotating-disk electrode (RDE, with a diameter of 5 mm) and rotating ring-disk electrode with glassy carbon disk (with a diameter of 5 mm) and Pt ring (RRDE) were both employed. The working electrode was prepared by coating a catalyst film onto the glassy carbon disk. The catalyst ink used in the coating was produced by dispersing 4 mg of catalyst in 2 mL of ethanol solution containing 16 μ L of 5 wt% Nafion (Alfa Aesar, D520 dispersion) and sonicated for 120 min. Proper amount of the as-obtained catalyst ink was coated onto the glassy carbon disk drop by drop to ensure a catalyst loading of 0.5 mg/cm², and then the as-obtained electrode was dried at room temperature overnight. The counter and reference electrodes are graphite rod and Ag/AgCl electrode (3.5 mol/L KCl) respectively. 0.1 mol/L KOH aqueous solution was used as electrolyte. Argon or oxygen was bubbling into the electrolyte 30 min prior the electrochemical tests according to the demands. All measured potentials were converted to potential vs. reversible hydrogen electrode (RHE) according to the following equation, unless specified [15,19]:

$$E_{\text{vs RHE}} = E_{\text{vs Ag/AgCl}} + E_{\text{o Ag/AgCl}} + 0.059 \text{ pH} \quad (1)$$

Where $E_{\text{vs RHE}}$ is the potential vs. RHE, $E_{\text{vs Ag/AgCl}}$ is the potential vs. Ag/AgCl and $E_{\text{o Ag/AgCl}}$ is the potential of Ag/AgCl electrode respect to the standard hydrogen electrode. The cycle voltammetry (CV) and linear sweep voltammetry (LSV) with a scan rate of 10 mV/s in the potential range from -0.025 V to 1.175 V vs. RHE. The Pt ring in RRDE was held at a constant potential of 1.2 V to measure the amount of H₂O₂ formed at the disk electrode during ORR. To compare with, a Pt/C (30 wt% Pt on Vulcan carbon black, Fuel Cell Store) ink was prepared and used to produce working electrodes with similar procedure described above.

For RDE tests, the electron transfer number (n) per oxygen molecule in ORR process at the electrode was calculated with the Koutechy-Levich (K-L) method [15,31]:

$$B = 0.2nFC_0D_0^{2/3}v^{1/6} \quad (2)$$

$$1/J = 1/J_L + 1/J_K = 1/(B\omega^{1/2}) + 1/J_K \quad (3)$$

Where J is the measured current density, J_L is the diffusion limiting current density, J_K is the kinetic limiting current density, ω is the rotating speed in rpm, F is the Faraday constant ($96,485 \text{ C mol}^{-1}$), D_0 is the diffusion coefficient of oxygen in 0.1 mol/L KOH ($1.9 \times 10^{-5} \text{ cm}^2 \text{ s}^{-1}$), v is the kinetic viscosity ($0.01 \text{ cm}^2 \text{ s}^{-1}$), and C_0 is the bulk concentration of oxygen ($1.2 \times 10^{-3} \text{ mol L}^{-1}$).

For RRDE tests, The % HO_2^- and n were determined by the followed equations [16–18]:

$$\% \text{HO}_2^- = 200(I_r N^{-1})(I_d + I_r N^{-1})^{-1} \quad (4)$$

$$n = 4I_d(I_d + I_r N^{-1})^{-1} \quad (5)$$

Where I_d is disk current, I_r is ring current and N is current collection efficiency of the Pt ring. N is determined to be 0.41 in our instrument.

The Turnover Frequency (TOF) is calculated from the equation [32–34]:

$$\text{TOF} = (j \times A)(4 \times F \times m)^{-1} \quad (6)$$

Where j is the current density at a given overpotential, A is the surface area of the electrode (0.196 cm^2), F is the Faraday constant ($96,485 \text{ C mol}^{-1}$) and m is the number of moles of metal on the catalyst surface. For our catalysts, we assume all Fe atoms are coordinated in active sites and each active sites hosts only one Fe atom. Thus, we used mole of metal on electrode for our catalyst instead.

3. Results and discussion

The electrocatalytic properties of Fe-NPC were investigated, and the results are presented in Fig. 1 and Figure S1 in supplementary information. Figure S1 demonstrated the CV curves of Fe-NPC and CWB in Ar-saturated or O_2 -saturated 0.1 mol/L KOH aqueous solution at a scan rate of 10 mV/s . Distinct reduction peaks can be observed only in the O_2 -saturated electrolyte, suggesting the abilities of these materials to catalyse oxygen reduction. Moreover, the ORR peak position of Fe-NPC, which is about 270 mV more positive than that of CWB, is similar to that of 30% Pt/C, indicating outstanding electrocatalytic activity of Fe-NPC towards oxygen reduction. LSV tests were carried out and the obtained curves are shown in Fig. 1a. The pure carbon CWB exhibited a poor ORR activity, almost inert for ORR, while the ORR activity of carbon doped with Fe, N and P (Fe-NPC) was enhanced remarkably, which is comparable to the activity of 30% Pt/C. The onset potentials (E_{onset}) and half-wave potentials (E_{half}) of each catalyst obtained from the LSV curves are presented in Fig. 1b. Both E_{onset} and E_{half} of Fe-NPC are similar to or even slightly more positive than those of 30% Pt/C. This result suggests that the Fe-NPC catalyst is a cost effective, highly

efficient catalyst as a promising alternative to the commercial Pt/C catalysts.

To reveal the origin of the ORR activity of Fe-NPC, different characterizations were carried out. The typical SEM image of Fe-NPC (Fig. 2a) shows highly porous structure with rough surface, and some large spherical particles are dispersed on the surface. Aberration-corrected HAADF-STEM images of Fe-NPC are shown in Fig. 2b and c, where the element mappings of C, N, P and Fe of the sample in Fig. 2b are shown in Fig. 2d, e, f and g, respectively. The large spherical particles are also observed in Fig. 2b, while these particles are highlighted in P and Fe mapping, indicating that they are majorly composed of Fe and P. The N dispersion is basically overlapped with the C dispersion, indicating the evenly doping of N on the carbon body. The Fe containing particles is about 100 nm , as it is also shown in the TEM images (Figure S2). A higher magnification TEM image (Figure S2b) demonstrates that these particles are encapsulated by carbon layers. Furthermore, distinct white dots with size around one angstrom can be observed in the atomic-resolution HAADF observations (partially indicated by red cycles in Fig. 2c), which is similar to the results of our previous works [35,36] and reported literatures [37,38], revealing that a significant number of Fe single atoms exist on Fe-NPC. The results indicate that Fe in Fe-NPC also has two types of existence form: particles and single atoms.

N_2 sorption analysis of Fe-NPC was carried out, and the resulted isotherms are shown in Figure S3a. The isotherm curve of Fe-NPC has a similar shape with type I isotherm, indicating that Fe-NPC is micropore abundant material. The pore size distributions (PSDs) of Fe-NPC is shown in Figure S3b. The peak of the PSD curve of Fe-NPC is at around 2 nm with 2 shoulders at around 1.6 and 2.7 nm , respectively. Fe-NPC possesses a SSA of $1361 \text{ m}^2/\text{g}$, a mesopore volume of $0.24 \text{ cm}^3/\text{g}$ and a micropore volume of $0.37 \text{ cm}^3/\text{g}$. The results suggest the formation of hierarchically porous structures, which is believed to be beneficial to the mass transfer and access of the active sites during oxygen reduction [19]. The XRD curves of Fe-NPC is shown in Figure S3c, where clear peaks ascribed to FeP or Fe_2P are found. Combining XRD and STEM mapping observations, spherical particles presented can be ascribed to iron phosphides, which are reported to possess reasonable ORR activities when encapsulated by carbon layers [39–42]. Moreover, the Fe and P loading of Fe-NPC were obtained from TPO and XRF analysis, which are calculated to be 2.67 wt \% and 1.83 wt \% , respectively.

The results of XPS analysis of Fe-NPC are shown in Fig. 3. Sharp peaks of C 1s and O 1s can easily be observed from the survey curve (Fig. 3a), while the peaks for N 1s and P 2p is much smaller. The elemental concentrations of Fe-NPC are shown in Table S1, where C, N, P and Fe atomic percentages are 89.29 , 2.18 , 0.42 and 0.59 , respectively. The deconvolutions of N 1s, P 2p and Fe 2p peaks of Fe-NPC were carried out, as shown in Fig. 3b-d. The concentrations of each component peaks (in at%) are summarized in Table S2. N 1s peak can

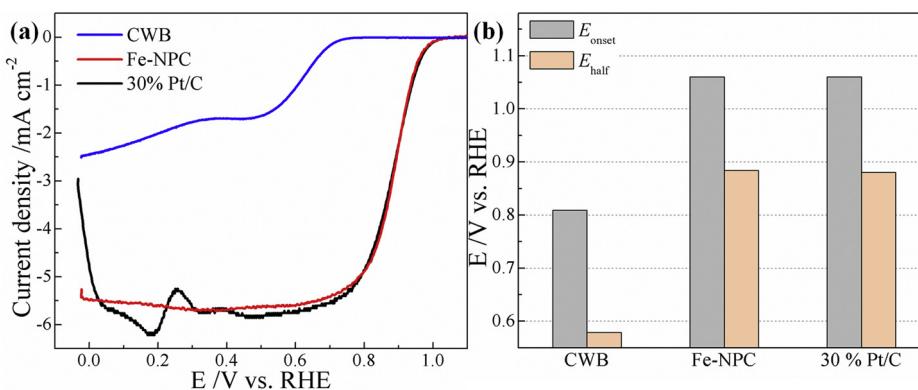


Fig. 1. (a) LSV curves of Fe-NPC, CWB and 30% Pt/C in O_2 -saturated 0.1 mol/L KOH at a scan rate of 10 mV/s with a rotating rate of 1600 r.p.m. (b) Bar chart of E_{onset} and E_{half} of Fe-NPC, CWB and 30% Pt/C.

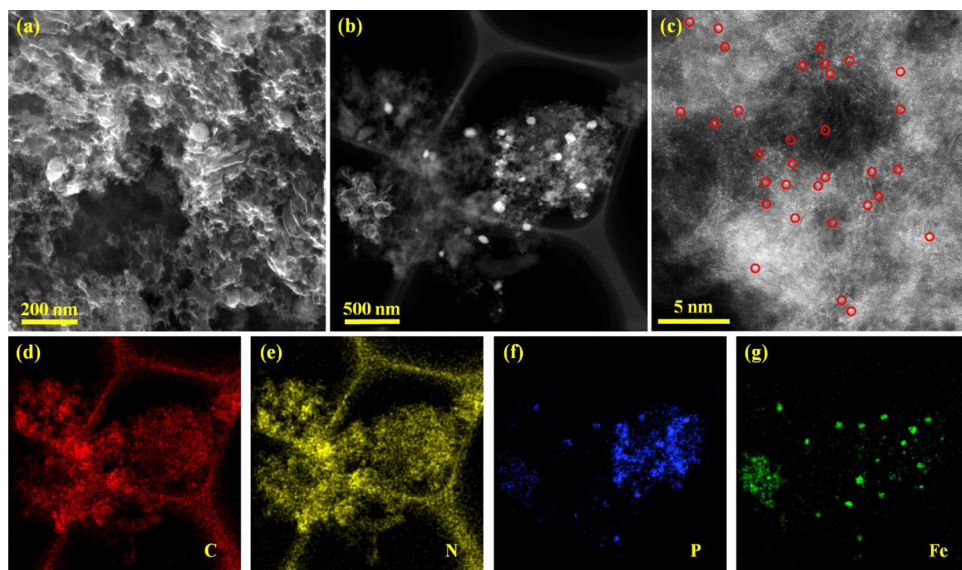


Fig. 2. (a) SEM image of Fe-NPC. (b and c) Aberration-corrected HAADF-STEM images of Fe-NPC, in which some of the isolated Fe atoms are highlighted by red circles in (c). Element mapping of (d) C, (e) N, (f) P and (g) Fe correlated to (b) (For interpretation of the references to colour in this figure legend, the reader is referred to the web version of this article).

be fitted into four peaks located at around 398.6, 400.5, 401.3 and 402.0 eV, which correspond to pyridinic N (N1), pyrrolic N (N2), graphitic N (N3) and oxidized pyridinic N (N4), respectively [15]. For Fe-NPC, the concentration for N1 and N2 are similar, and the existence of pyridinic N (N1) is reported to be highly related to the activity of the catalysts towards oxygen reduction [14,15,43]. P 2p peaks can be deconvoluted into five peaks locate at around 132.9, 133.8, 135.5, 129.3 and 130.2 eV, which are aroused by P–C bond (P1), P–O bond (P2), metaphosphate (PO_3^- , P3), P 2p_{3/2} of P-Fe (P4) and P 2p_{1/2} of P-Fe (P5), respectively [17,44,45]. The present of P1 peak suggests that P is successfully doped into carbon body of Fe-NPC, while the existences of

P4 and P5 suggest the present of P-Fe bond, which are possibly ascribed to the Fe_xP particles. In the Fe 2p region, clear peaks for Fe 2p_{3/2} and Fe 2p_{1/2} can be found in Fe-NPC spectrum, although the noise level is relatively high due to the low Fe content. These two peaks can be fitted into five peaks located at around 710.5 eV, 712.5 eV, 718 eV, 724.2 eV and 726.2 eV, which are ascribed to the Fe 2p_{3/2} of Fe^{2+} (Fe1) and Fe^{3+} (Fe2), satellite peak of Fe2p_{3/2} (Fe3) and Fe 2p_{1/2} of Fe^{2+} (Fe4) and Fe^{3+} (Fe5), respectively [46,47]. No peaks for element Fe can be found. Although it is difficult to get quantitative distribution of different Fe species due to relatively noise level, these results suggest that the Fe single atoms displayed in Fig. 2c are existed in the form of

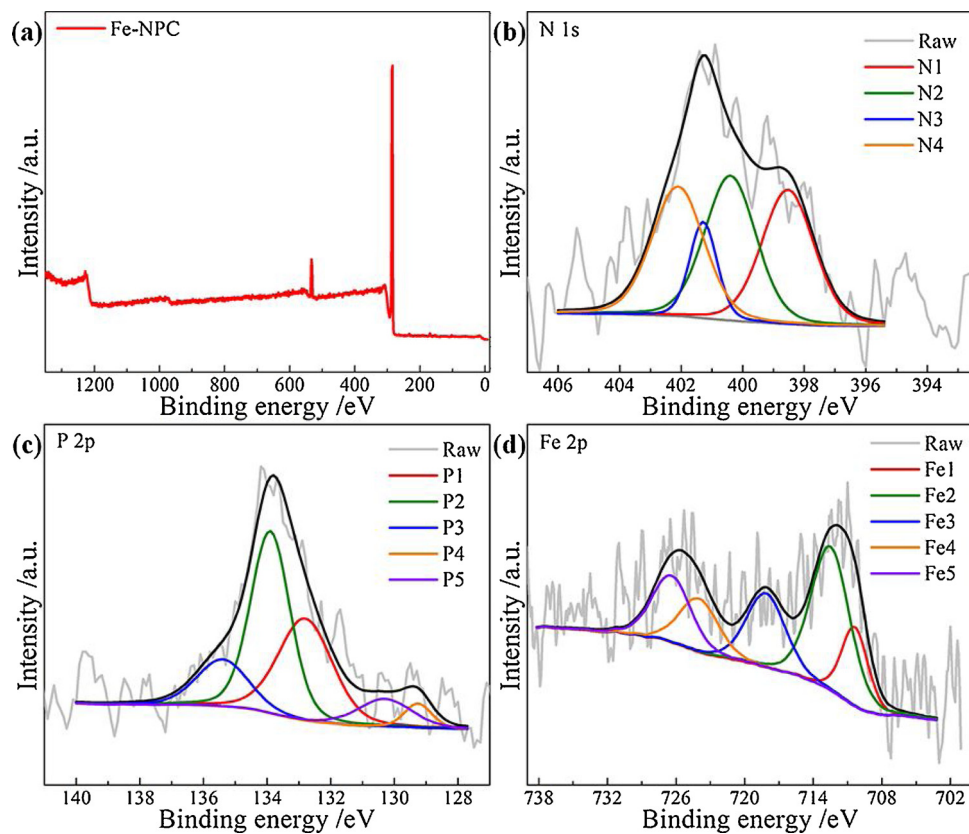


Fig. 3. (a) XPS survey, (b) N 1s peak, (c) P 2p peak and (d) Fe 2p peak of Fe-NPC.

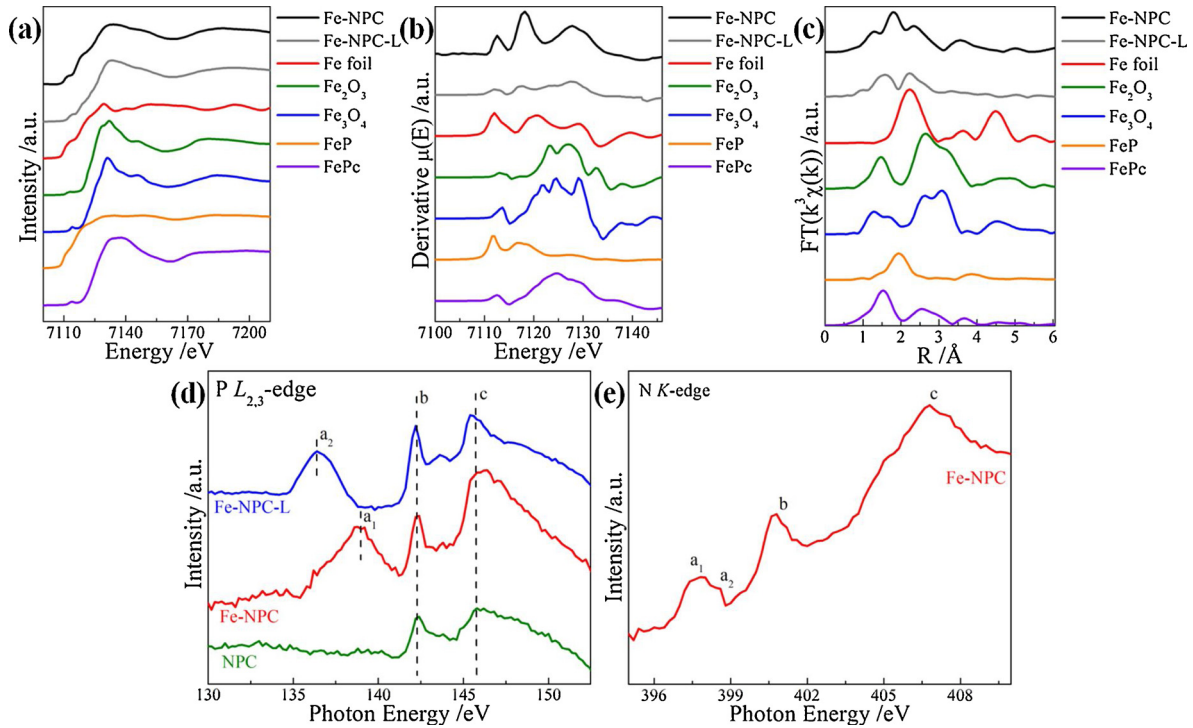


Fig. 4. (a) Fe K-edge XANES spectra, (b) corresponding first derivative analysis and (c) the k^3 weighted $\chi(k)$ function of the EXAFS spectra for Fe-NPC, Fe-NPC-L, Fe foil, Fe_2O_3 , Fe_3O_4 , FeP and FePc. (d) P $L_{2,3}$ -edge XANES spectra of Fe-NPC, Fe-NPC-L and NPC. (e) N K-edge XANES spectra of Fe-NPC.

bivalent and/or trivalent ions.

The synchrotron-based X-ray absorption fine structure spectroscopy (XAFS) technique was employed to acquire more information on the local structure and bonding of the absorbing atom in as-prepared catalysts. Fig. 4a shows the normalized Fe K-edge XANES spectra of Fe-NPC, and reference materials of Fe_2O_3 , Fe_3O_4 , FeP, iron phthalocyanine (FePc) and Fe foil. For a clarity purpose, the spectra of the reference materials, a comparison of Fe-NPC with FePc and a comparison of Fe-NPC-L with FeP and FePc are presented in Figure S4, S5 and S6, respectively. In their corresponding first derivative analysis in Fig. 4b and Figure S10, the existence of small pre-edge featured at 7112.5 eV in FePc is attributed to a dipole-forbidden but quadrupole-allowed $1s \rightarrow 3d$ transition in a square planar of FeN_4 [48]. The pre-edge of Fe-NPC located the similar position, but the intensity is much higher compared to the one of FePc (Fig. 4b and Figure S11b). In the absorption edges (~ 7120 – 7140 eV), FePc reference exhibits the most dominant feature of several $1s \rightarrow 4p$ transitions, which are characteristic of an iron (II) complex with square-planar configuration [49,50]. The adsorption edge of Fe-NPC exhibited completely different from the FePc (Figure S11). Both pre edge and adsorption edge located between Fe and Fe (II) in the FeN_4 . It clearly reveals a new structure of active site instead of FeN_4 on Fe-NPC.

For the analysis of extended X-ray absorption fine structural (EXAFS) spectroscopy, Fourier transformations (FT) of the k^3 -weighted EXAFS functions observed for Fe-NPC and reference compounds are shown in Fig. 4c. A comparison of EXAFS spectra between Fe-NPC and Fe-Pc is presented in Figure S11c, which further confirms a different surrounding structure of Fe in Fe-NPC compared to the one in FePc. The first peak at around 1.30 \AA in Fig. 4c and Figure S11 for Fe-NPC could be assigned to the Fe-N/O distance, suggesting the existence of the Fe-N and Fe-O coordinations, which reveals single Fe atoms existing in the catalysts. The second peak appeared at around 1.80 \AA , which is shorter than the Fe-P distance in FeP ($\sim 1.94 \text{ \AA}$, Fig. 4b green curve) and longer than the Fe-P distance in Fe_2P (1.75 \AA) [51]. This peak can be ascribed to Fe-P coordination in Fe-NPC. The third peak ($\sim 2.34 \text{ \AA}$) is ascribed to Fe-Fe distance, which is slightly shifted from the Fe-Fe distance of

element Fe ($\sim 2.23 \text{ \AA}$) to that of Fe_2O_3 ($\sim 2.64 \text{ \AA}$). This could be the evidence of the existence of iron oxide with low valent Fe, which may be the result of mild oxidation when the catalyst contacted with air. Combining the XPS and EXAFS characterizations, Fe single atoms may coordinate to O, N and P simultaneously, and N and P are both binding to C. However, due to complicated structure, it is not able to obtain accurate coordination numbers of Fe with different surround elements.

Fig. 4d shows a completely distinct P $L_{2,3}$ -edge XANES spectra for each catalyst after the phosphorus modification. A broad and intense peak (peak c) at 145.8 eV can be observed in all spectra, owing to the 2p to 3d transitions in phosphorous [52]. The feature (peak b) at 142.3 eV may be ascribed to the P–C/N bonds, suggesting the P heteroatom was successfully doped into carbon matrix [53]. More interestingly, the Fe-NPC catalyst shows another peak (peak a₁) at 138.8 eV with a weak shoulder compared to that of NPC, which is attributed to the transitions to 3p orbitals. It is possible due to the mixed characters from oxygen or metals and forms the Fe–O–P bond [54,55]. The existence of Fe–O–P bond further confirm the present of Fe–O and P–O bond. Notably, we have used the total electron yield (TEY) mode to collect all XANES spectra, which is sensitive to the surface with detection depth \sim 5–10 nm [56]. Thus, the iron phosphate could be detected in the Fe_xP -contained Fe-NPC catalyst due to the surface oxidation in the air. When the Fe content in the catalyst was reduced to form the atomically dispersed catalyst (Fe-NPC-L), the peak was shifted to the lower energy side at 136.4 eV (peak a₂). It is mainly due to the increase in more covalent P–C bonds when the Fe atoms were trapped into carbon matrix in the isolated form. The C atoms possesses smaller electronegativity than the O atom, where the change in the degree of covalence of the P–O bond altered by more contributions of P–C bonds.

N K-edge XANES spectra in Fig. 4e reflects the unoccupied N 2p electronic states. The peaks at about 398.2 eV (peak a) is assigned to π^* transition to pyridinic state, while other two peaks at 401.0 eV (peak b) and 406.9 eV (peak c) are assigned to graphitic N and C–N σ^* transitions, respectively [57]. Noteworthy, the peak a splits into double peaks (labeled as a₁ and a₂) suggests that Fe is bonded to pyridinic N, agreeing with the previous report [58] and confirming the Fe–N coordination.

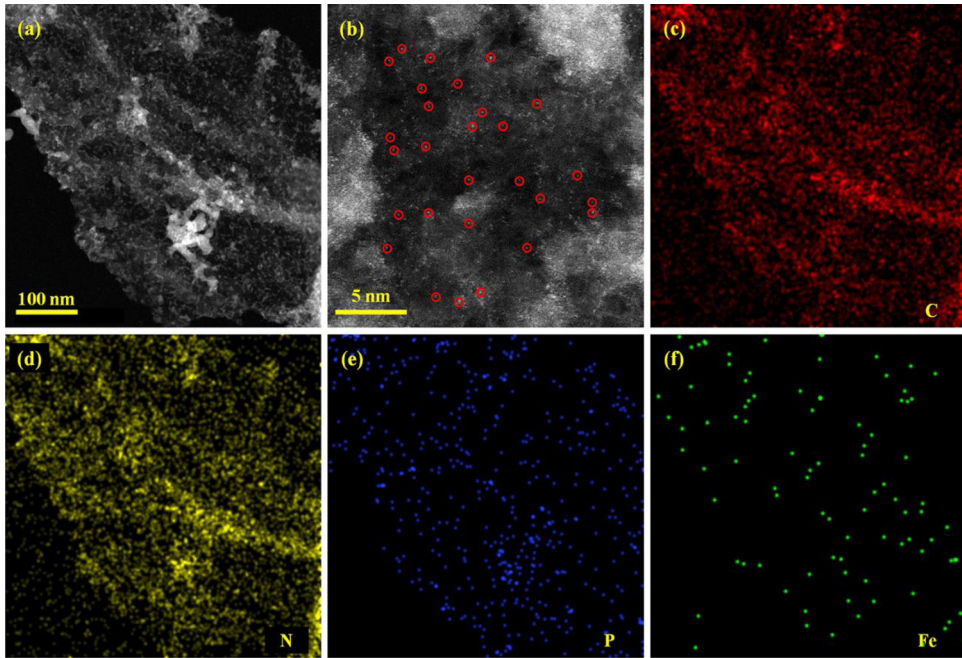


Fig. 5. Aberration-corrected HAADF-STEM images and element mappings of Fe-NPC-L. Some of the isolated Fe atoms are highlighted by red circles in (b) (For interpretation of the references to colour in this figure legend, the reader is referred to the web version of this article).

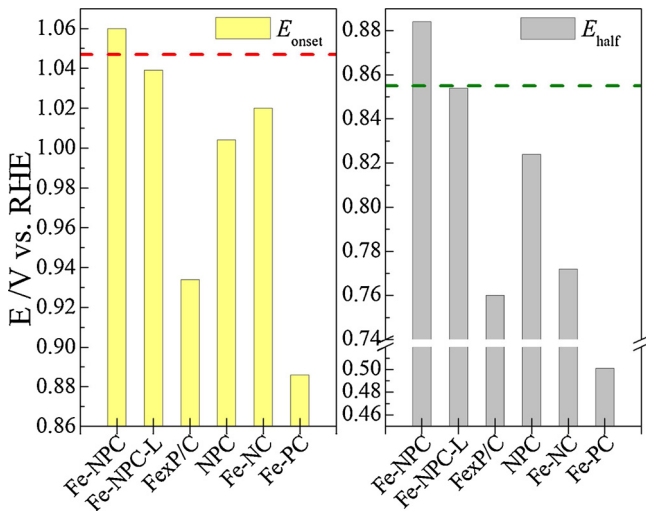


Fig. 6. E_{onset} and E_{half} of NPC, Fe_xP/C, Fe-NC, Fe-NPC-L and Fe-NPC. Red and green dash line represent the E_{onset} and E_{half} of 30% Pt/C, respectively (For interpretation of the references to colour in this figure legend, the reader is referred to the web version of this article).

All above characterizations revealed the formation of Fe–N, Fe–P, Fe–O–P, N–C and P–C bonds on the surface of Fe-NPC, which may be highly related to the good ORR activity of Fe-NPC displayed above. To further assess the contribution of each dopants (Fe, N, and P), and to exclude the effect of Fe_xP particles towards the overall activity, Fe-NPC-L (with lower Fe loading), Fe_xP/C (with higher Fe loading), NPC (without Fe), Fe-NC (without P) and Fe-PC (without N) were employed as reference catalysts. The detailed Fe and P loadings of these materials were also obtained from the XRF and TPO analysis and the results are shown in Table S3. The aberration-corrected HAADF-STEM images of Fe-NPC-L are shown in Fig. 5. No obvious particles can be observed in the dark field image of Fe-NPC-L, which may be owing to the low Fe and P loadings. In the element mapping, C, N, P and Fe are all evenly distributed throughout the whole catalyst, and no accumulation can be observed. Fe single atoms can still be observed in high-magnification

images (Fig. 5b). The results suggest that Fe is uniformly distributed as single atoms on Fe-NPC-L.

XPS survey of Fe-NPC-L is shown in Figure S4a, and the element concentrations are summarized in Table S1. The deconvolution of N 1s, P 2p and Fe 2p peaks of Fe-NPC-L are shown in Figure S4b-d and related component peak concentrations are summarized in Table S2. Since Fe-NPC-L was produced with the same method of Fe-NPC, the single Fe atoms on Fe-NPC-L should possess similar coordination to O, N and P and all related bonds are also formed on the surface. It is confirmed by the XANES spectra of Fe-NPC-L very similar to the one of Fe-NPC as shown in Fig. 4a and b, and more detailed plot in Figure S12, in which there are two peaks with similar area that can be possibly assigning to Fe-N and Fe-P (Figure S12c). Thus, Fe-NPC-L is a material similar to Fe-NPC but without Fe_xP particles.

Detailed characterizations of Fe_xP/C, NPC, Fe-NC and Fe-PC are presented in supplementary information (sections S3-S6, respectively, and Figure S8-S13), the results of which suggested the successful production of Fe_xP particle abundant materials and exclusion of each dopants.

The LSV curves of these catalysts are shown in Figure S14. It can be easily observed that the ORR activities of these catalysts decrease in an order of Fe-PC < Fe_xP/C < Fe-NC < NPC < Fe-NPC-L ≈ 30% Pt/C < Fe-NPC and the comparison of the E_{onset} and E_{half} of these materials is shown in Fig. 6. The Fe_xP/C (with high amount of Fe_xP particles) showed poor activity, much worse than it of Fe-NPC-L, which suggests that Fe_xP particles have minor contribution to the total activity of Fe-NPC. Meanwhile, Fe_xP/C, NPC, Fe-NC and Fe-NPC-L possess similar pyridinic N concentration (higher than that of Fe-NPC), but these materials showed very different activity, suggesting that pyridinic N concentration is not a determining factor for the ORR activity of Fe-NPC. When the single Fe atoms are integrated into N-P co-doped carbon (Fe-NPC-L), the activity boosted significantly, which is even comparable to that of 30% Pt/C. The TOF of Fe-NPC-L (with only Fe single atoms) was calculated to be 0.79 s^{-1} at 0.8 V vs. RHE. A comparison between the TOF of our catalyst and reported catalysts were carried out and summarized in Table S4. The TOF of Fe-NPC-L is larger than catalysts with similar or even higher Fe loadings. Although the TOF value is lower than Pt reference, it is acceptable as the cost of our catalysts are much

lower than Pt catalyst with 47 wt% loading. When either of the dopants is missing (NPC without Fe, Fe-NC without P and Fe-PC without N), the ORR activity was diminished. This result suggests the synergy effect between all dopants, e.g., Fe, N and P, and thus the related Fe–N, Fe–P, Fe–O–P, N–C and P–C bonds is believed to form a unique atomically dispersed Fe-N-P-C complex with Fe as active centers, which is highly active for ORR reaction. The proposed structure of the Fe-N-P-C complex is shown in Figure S15. The activity of materials possessing both encapsulated Fe_{x}P particles and Fe-N-P-C complex structures were further enhanced and thus led to an outstanding ORR activity.

To gain further insights into the superior ORR activity of the unique atomically dispersed Fe-N-P-C complex structure, we resorted to first-principles calculations using density functional theory (DFT) methods (more computational details are shown in supplementary information). Based on the experimental determined structure characters of single Fe site, co-existing Fe–N, Fe–P, N–C and P–C bonds but without typical MN4 structure, together with a consideration of the fact that nitrogen and phosphorus atoms, in particular due to the large size of P, prefer to substitute the C atoms near the edge [59,60], we constructed the corresponding N-P-Fe structure in carbon as shown in Figure S16a. Meanwhile, a classic model of Fe-N₂ coordination structure (Figure S16b) was also constructed as a reference for a comparison. Due to the high electronegativity of the iron and the phosphorus, Fe–O, P–O and Fe–O–P bond always exist in the Fe-P composite when exposed to the air during the preparation and the reaction [17,61]. These oxygen containing bonds have been also observed on the Fe-N-P-C samples by the XPS and XANES characterization as discussed above. In addition, it has been reported that the oxygen associated to the Fe site could play an important role in the activity for the iron-based ORR catalyst [62]. Therefore, 1, 2 and 3 oxygen coordinated with the two basic structures (N-P-Fe and Fe-N₂) are also established as shown in Figure S16. The relative stability of these structures was investigated by DFT in terms of the oxygen formation energy or oxygen binding energy and their relative stability was summarized in Table S5. Fig. 7a shows that the oxygen formation energy (E_{O}) of both the Fe-N-P-C and Fe-N-C model catalysts increases with increasing the coordinated O atoms from 1 to 4,

but depends clearly on the structure of active site, namely N-P-Fe and N₂-Fe. In general, the oxygen formation energy is lower on the N-P-Fe than on the N₂-Fe structures, possibly due to both P and Fe having a high affinity to oxygen. Coordination of P into the structure clearly lowers the oxygen formation heat and increases the O stability. Fig. 7a indicates that the structure coordinated with higher number of O is not energetically favourable, and more energy required for the formation of the structures. The results suggest that up to two O coordinated N-P-Fe structure (N-P-O-Fe-O) and one O coordinated N₂-Fe structure (N₂-Fe-O) are energetically favourable for the formation. Owing to the strong affinity to oxygen for Fe, the single Fe is always coordinated at least one oxygen. More interestingly, inserting second oxygen to the N-P-Fe-O yielded the most stable structure of N-P-O-Fe-O (Figure S16e), and preferably formed P–O–Fe bond, which is in good agreement with the experimental observation.

As it has been reported that Fe sites are more likely to be the active site for ORR compare to N or C site [62], we further investigated the oxygen reduction progress based on the associative mechanism in alkaline media (equation S1-S6 in supporting information) on the Fe sites in various active site structures. Fig. 7b shows the resulted free energy profiles on these active sites at the equilibrium potential. Since the ORR overpotential (η_{ORR}) is an important measure of the catalytic activity of a catalyst [63], the theoretical overpotentials of these three models for ORR were obtained from the correlated free energy profiles and compared in a bar chart (Fig. 7c). N₂-Fe site without coordination of oxygen has the highest overpotential, while N-P-O-Fe-O with Fe–O–P and Fe–O bond possesses the lowest overpotential and thus the highest ORR activity among all the active sites studied. The rate determining step for these models is the desorption of OH*, which is similar to it on the Pt (111) surface [64,65].

To further understand the physical basis of the superior activity of the N-P-O-Fe-O, the key electronic properties of the various active sites in principle determining the catalytic properties [66] were further analysed. A linear relationship between the G_{OH^*} and the Fe charge was unambiguously observed in Fig. 7d, suggesting Fe charge as an adequate descriptor for the ORR activity. Qualitatively, a more positive

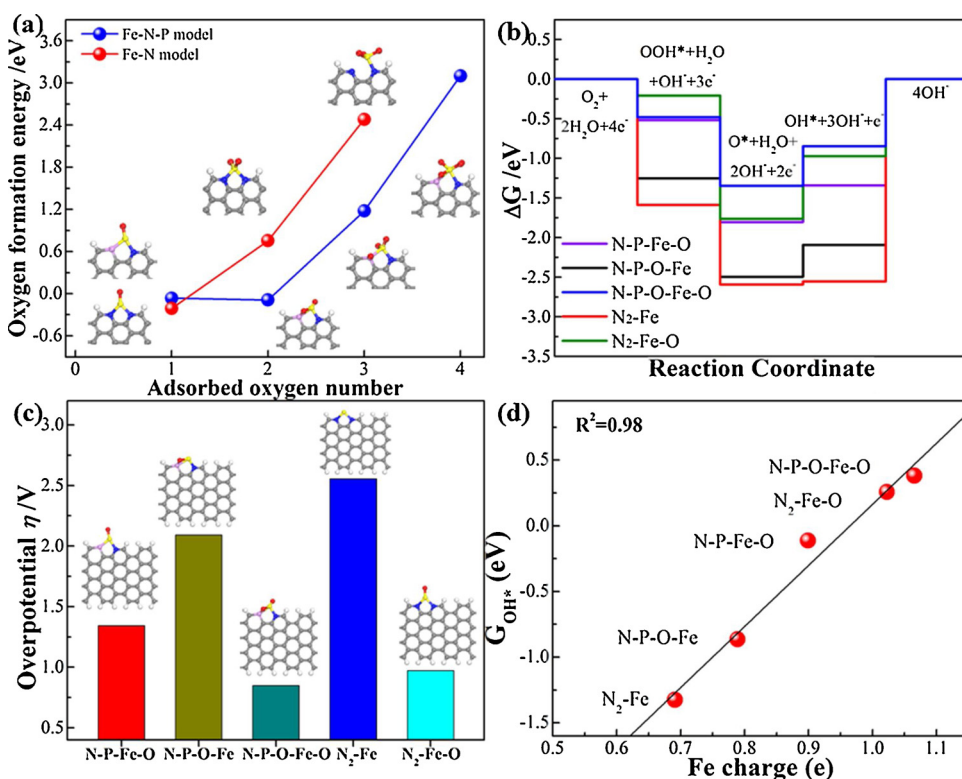


Fig. 7. (a) Oxygen formation energy for different models of Fe-P-N-C (blue dots) and Fe-N-C (red dots), in which insets indicate the corresponding oxygen adsorption configurations. (b) Free energy diagram for oxygen reduction reaction on the N-P-Fe-O, N-P-Fe, N-P-O-Fe-O, N₂-Fe and N₂-Fe-O models at the equilibrium potential ($U = 0.40 \text{ V vs. NHE}$). (c) The calculated ORR overpotentials (η_{ORR}) of these catalysts. (d) Trend in the adsorption free energy of OH* (G_{OH^*}) as a function of the Bader charge of the Fe atom of these models (For interpretation of the references to colour in this figure legend, the reader is referred to the web version of this article).

charge of the Fe atoms leads to a more mediate OH^* adsorption (larger value of G_{OH^*}), and thus to facilitate the overall ORR performance. The descriptor can rationalize the experimental determined ORR rate order: Fe-P-N-C > Fe-N-C. The unique structure of N-P-O-Fe-O enlarges the Fe charge. Moreover, results (Fig. 7d) reveal that the Fe charge depends significantly on the surrounding structure of active sites, and the descriptor could unify the structure effect of the active sites. On the other hand, it opens a new avenue for rational design of ORR catalyst through tuning the Fe charge by manipulating the surrounding local environments of the active sites, like a mimic of natural catalysts such as cytochrome c oxidase [27]. These results clearly demonstrated that the surrounding structure such as N, O and P coordinated to Fe combined with the dynamic process of the Fe–O–P bond during ORR contribute to the best ORR activity of the Fe-N-P-C catalyst among the catalyst studied in this work. It should be noted that the ORR activity in this work is still slightly lower than the best one in literature. However, it is anticipated that the ORR activity can be further increased by optimizing preparation methods to enrich the active sites, considering that the catalysts here prepared directly from woody biomass has relatively low active site number.

The catalytic cycle of the ORR and the optimized configurations of the intermediates involved on the N-P-O-Fe-O active sites (Fig. 8) were further analysed to reveal the origin of its high ORR activity. At the ORR equilibrium potential, the formation of OOH^* is exothermic, and ΔG is rather negative, suggesting a very fast reaction. Meanwhile, the O–O bond length is elongated to 1.42 Å for the OOH^* , which allows an easy dissociation of O–O bond in the subsequent steps. This is further evidenced by the fact that the dissociation of OOH^* to O^* is strongly exothermic. The hydrogenation of O^* is endothermic and the removal of OH^* is even more endothermic, suggesting that the step of OH^* removal is the rate-determining step that determines the overall ORR activity. It reveals a highly dynamic nature of the active site and a redox cycle between N-P-Fe-O₂ and N-P-Fe-O₃. Interestingly, the Fe–O–P bond of the N-P-O-Fe-O model would break to form the isolated P–O bond

during the ORR reaction and then Fe–O–P bond would be restored when an ORR catalytic cycle finished. During this dynamic redox process, the removal of OH^* is facilitated by Fe–O–P cycle, which leads to better ORR activity.

The electron transfer number was calculated from the as-obtained LSV curves with different rotating speed and the related K-L plots, which are shown in Figures S17 and S18a. All K-L plots exhibit linear relationships between J^{-1} and $\omega^{-1/2}$, the average electron transfer number for Fe-NPC is 3.90, slightly lower than that of 30% Pt/C (3.95). RRDE test is carried out to verify the electron transfer number and determine the H_2O_2 yield, as shown in Figure S18b. The curve obtained here is similar to those obtained with RDE tests that the E_{onset} (1.089 V vs. RHE) and E_{half} (0.883 V vs. RHE) are both similar to those obtained from RDE tests, confirming the good activity of Fe-NPC. Base on the RRDE curves, the H_2O_2 yield is about 3.72% and the average electron transfer number is estimated to be 3.93, which is very close to 3.90 determined by RDE tests. The Results obtained from K-L plots and RRDE test suggest that the ORR catalysed by Fe-NPC is carried out via an efficient four-electron pathway.

CVs of Fe-NPC and 30% Pt/C with a scan rate of 0.1 V/s were carried out for 5000 cycles, and the CV curves of them before and after cycling are shown in Figure S18c. Obvious shape and reduction peak position changes can be observed from the curves of Pt/C. The peak position shifted 45 mV towards negative after cycling, indicating a poor long-term stability. While the curves of Fe-NPC before and after cycling almost overlap and the ORR peak position remain the same. This result suggests a good stability for long-term oxygen reduction of Fe-NPC. Additionally, current-time curves at 0.7 V of Fe-NPC and Pt/C were recorded and 3 M CH_3OH was introduced after 400 s (indicated by the arrow), the results are shown in Figure S18d. Suffering the crossover effect, the current of Pt/C dropped dramatically after methanol was injected, only about 50% of its initial current remained. While for Fe-NPC, the addition of methanol only affected the current density slightly when it was introduced and the current restored after 100 s. The

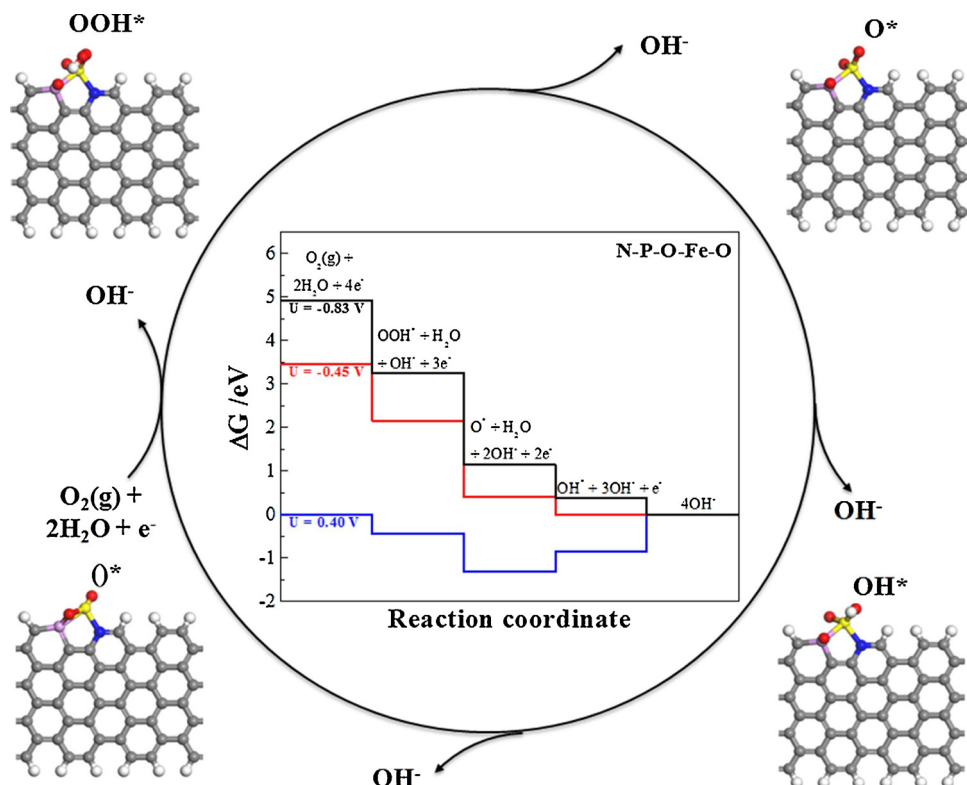


Fig. 8. Schematic of the ORR on the N-P-O-Fe-O catalyst. The inset in cycle shows the free energy diagram for oxygen reduction reaction on this catalyst in alkali medium. For $U < -0.45$ V (vs. NHE), all steps are thermodynamically accessible.

mechanism of the good stability and methanol tolerance of Fe-NPC will be further investigated in our future researches.

4. Conclusions

All above results from both experiments and DFT calculations indicate that atomically dispersed Fe-N-P-C electrocatalyst derived from biomass is a highly efficient, durable, best cost effective catalyst for electrochemical oxygen reduction ORR, making it one of the most promising replacement of traditional Pt-based electrocatalysts for sustainable, large-scale applications in electrochemical energy technologies such as fuel cells and metal-air batteries. A simple, cost effective and sustainable method for fabrication of atomically dispersed Fe catalysts directly from woody biomass is reported. In addition, we report the rational design principle of ORR catalysts for enhancing the ORR activity of single Fe site catalysts with the Fe charge as a descriptor, and the higher Fe charge resulted in the higher activity. We demonstrate a strategy of mimicking nature catalysts to tune the Fe charge by manipulating the associated coordination and ligands. We revealed a new molecule-like structure of the atomically dispersed Fe-N-P-C complex as the dominant active site for the ORR reaction by means of combined aberration-corrected HAADF-STEM, XPS and XAFS measurements and DFT calculations. We have identified the redox cycle between N-P-O-Fe-O and N-P-O-Fe-O₂ in the catalyst, and revealed the advantages of doping of P into the nitrogen carbon structure and thermodynamically favorable formation of Fe-O-P band by exposing P-Fe bond to oxygen during the preparation or reaction. The associated Fe-O-P bond plays a key role in enlarging Fe charge, lowering the stability of strongly adsorbed OH* on the active sites, and thus enhancing the ORR performance. Moreover, we rationalize the outperformance of Fe-N-P-C than Fe-N-C, and N-C. The strategy demonstrated here opens a new avenue for constructing highly efficient molecule-like heterogeneous catalysts in electrochemical energy technologies.

Competing financial interest

The authors declare no competing financial interest.

Acknowledgements

The financial supports from Department of Chemical Engineering, NTNU and Norwegian research council are highly acknowledged. Dr. Yahao Li acknowledges the support from China Scholarship Council (CSC) for his study at NTNU.

Appendix A. Supplementary data

Supplementary material related to this article can be found, in the online version, at doi:<https://doi.org/10.1016/j.apcatb.2019.03.016>.

References

- [1] A. Miura, C. Rosero-Navarro, Y. Masubuchi, M. Higuchi, S. Kikkawa, K. Tadanaga, Nitrogen-rich manganese oxynitrides with enhanced catalytic activity in the oxygen reduction reaction, *Angew. Chem. Int. Ed.* 55 (2016) 7963–7967.
- [2] M.D. Allendorf, Oxygen reduction reaction: a framework for success, *Nat. Energy* 1 (2016) 16058.
- [3] M. Lefèvre, E. Proietti, F. Jaouen, J.P. Dodelet, Iron-based catalysts with improved oxygen reduction activity in polymer electrolyte fuel cells, *Science* 324 (2009) 71–74.
- [4] K. Gong, F. Du, Z. Xia, M. Durstock, L. Dai, Nitrogen-doped carbon nanotube arrays with high electrocatalytic activity for oxygen reduction, *Science* 323 (2009) 760–764.
- [5] S. Yasuda, A. Furuya, Y. Uchibori, J. Kim, K. Murakoshi, Iron-nitrogen-doped vertically aligned carbon nanotube electrocatalyst for the oxygen reduction reaction, *Adv. Funct. Mater.* 26 (2016) 738–744.
- [6] L. Dai, Y. Xue, L. Qu, H.J. Choi, J.B. Baek, Metal-free catalysts for oxygen reduction reaction, *Chem. Rev.* 115 (2015) 4823–4892.
- [7] L. Yu, X. Pan, X. Cao, P. Hu, X. Bao, Oxygen reduction reaction mechanism on nitrogen-doped graphene: a density functional theory study, *J. Catal.* 282 (2011) 183–190.
- [8] L. Dubau, J. Nelayah, S. Moldovan, O. Ersen, P. Bordet, J. Drnec, T. Asset, R. Chattot, F. Maillard, Defects do catalysis: CO monolayer oxidation and oxygen reduction reaction on hollow PtNi/C nanoparticles, *ACS Catal.* 6 (2016) 4673–4684.
- [9] D.S. Choi, A.W. Robertson, J.H. Warner, S.O. Kim, H. Kim, Low-temperature chemical vapor deposition synthesis of Pt-Co alloyed nanoparticles with enhanced oxygen reduction reaction catalysis, *Adv. Mater.* 28 (2016) 7115–7122.
- [10] K.H. Choi, Y. Jang, D.Y. Chung, P. Seo, S.W. Jun, J.E. Lee, M.H. Oh, M. Shokouhimehr, N. Jung, S.J. Yoo, Y.E. Sung, T. Hyeon, A simple synthesis of urchin-like Pt-Ni bimetallic nanostructures as enhanced electrocatalysts for the oxygen reduction reaction, *Chem. Commun.* 52 (2016) 597–600.
- [11] K.A. Kuttiyiel, K. Sasaki, G.G. Park, M.B. Vukmirovic, L. Wu, Y. Zhu, J.G. Chen, R.R. Adzic, Janus structured Pt-FeNC nanoparticles as a catalyst for the oxygen reduction reaction, *Chem. Commun.* 53 (2017) 1660–1663.
- [12] H. Yu, L. Shang, T. Bian, R. Shi, G.I. Waterhouse, Y. Zhao, C. Zhou, L.Z. Wu, C.H. Tung, T. Zhang, Nitrogen-doped porous carbon nanosheets templated from g-C₃N₄ as metal-free electrocatalysts for efficient oxygen reduction reaction, *Adv. Mater.* 28 (2016) 5080–5086.
- [13] L. Tao, Q. Wang, S. Dou, Z. Ma, J. Huo, S. Wang, L. Dai, Edge-rich and dopant-free graphene as a highly efficient metal-free electrocatalyst for the oxygen reduction reaction, *Chem. Commun.* 52 (2016) 2764–2767.
- [14] J. Zhang, L. Qu, G. Shi, J. Liu, J. Chen, L. Dai, N. P-codoped carbon networks as efficient metal-free bifunctional catalysts for oxygen reduction and hydrogen evolution reactions, *Angew. Chem. Int. Ed.* 55 (2016) 2230–2234.
- [15] J. Zhang, Z. Zhao, Z. Xia, L. Dai, A metal-free bifunctional electrocatalyst for oxygen reduction and oxygen evolution reactions, *Nat. Nanotechnol.* 10 (2015) 444–452.
- [16] A. Muthukrishnan, Y. Nabae, T. Okajima, T. Ohsaka, Kinetic approach to investigate the mechanistic pathways of oxygen reduction reaction on Fe-containing N-doped carbon catalysts, *ACS Catal.* 5 (2015) 5194–5202.
- [17] K.P. Singh, E.J. Bae, J.S. Yu, Fe-P: a new class of electroactive catalyst for oxygen reduction reaction, *J. Am. Chem. Soc.* 137 (2015) 3165–3168.
- [18] Y. Liang, Y. Li, H. Wang, J. Zhou, J. Wang, T. Regier, H. Dai, Co₃O₄ nanocrystals on graphene as a synergistic catalyst for oxygen reduction reaction, *Nat. Mater.* 10 (2011) 780–786.
- [19] M. Ma, S. You, W. Wang, G. Liu, D. Qi, X. Chen, J. Qu, N. Ren, Biomass-derived porous Fe₃C/tungsten carbide/graphitic carbon nanocomposite for efficient electrocatalysis of oxygen reduction, *ACS Appl. Mater. Interfaces* 8 (2016) 32307–32316.
- [20] W.J. Jiang, L. Gu, L. Li, Y. Zhang, X. Zhang, L.J. Zhang, J.Q. Wang, J.S. Hu, Z. Wei, L.J. Wan, Understanding the high activity of Fe-N-C electrocatalysts in oxygen reduction: Fe/Fe₃C nanoparticles boost the activity of Fe-N_x, *J. Am. Chem. Soc.* 138 (2016) 3570–3578.
- [21] R. Li, Z. Wei, X. Gou, Nitrogen and phosphorus dual-doped graphene/carbon nanosheets as bifunctional electrocatalysts for oxygen reduction and evolution, *ACS Catal.* 5 (2015) 4133–4142.
- [22] G.A. Ferrero, K. Preuss, A. Marinovic, A.B. Jorge, N. Mansor, D.J. Brett, A.B. Fuertes, M. Sevilla, M.M. Titirici, Fe-N-Doped carbon capsules with outstanding electrochemical performance and stability for the oxygen reduction reaction in both acid and alkaline conditions, *ACS Nano* 10 (2016) 5922–5932.
- [23] X. Cui, S. Yang, X. Yan, J. Leng, S. Shuang, P.M. Ajayan, Z. Zhang, Pyridinic-nitrogen-dominated graphene aerogels with Fe-N-C coordination for highly efficient oxygen reduction reaction, *Adv. Funct. Mater.* 26 (2016) 5708–5717.
- [24] C. Zhu, S. Fu, J. Song, Q. Shi, D. Su, M.H. Engelhard, X. Li, D. Xiao, D. Li, L. Estevez, D. Du, Y. Lin, Self-assembled Fe-N-Doped carbon nanotube aerogels with single-atom catalyst feature as high-efficiency oxygen reduction electrocatalysts, *Small* 13 (2017) 1603407.
- [25] J. Wang, K. Wang, F.B. Wang, X.H. Xia, Bioinspired copper catalyst effective for both reduction and evolution of oxygen, *Nat. Commun.* 5 (2014) 5285.
- [26] J. Suntivich, H.A. Gasteiger, N. Yabuuchi, H. Nakanishi, J.B. Goodenough, Y. Shao-Horn, Design principles for oxygen-reduction activity on perovskite oxide catalysts for fuel cells and metal-air batteries, *Nat. Chem.* 3 (2011) 546.
- [27] E. Kim, M.E. Helton, I.M. Wasser, K.D. Karlin, S. Lu, H.W. Huang, P. Moënne-Locoz, C.D. Incarvito, A.L. Rheingold, M. Honecker, Superoxide, μ -peroxy, and μ -oxo complexes from heme/O₂ and heme-Cu/O₂ reactivity: Copper ligand influences in cytochrome c oxidase models, *Proc. Natl. Acad. Sci.* 100 (2003) 3623–3628.
- [28] J.H. Zagal, M.T. Koper, Reactivity descriptors for the activity of molecular MN₄ catalysts for the oxygen reduction reaction, *Angew. Chem. Int. Ed.* 55 (2016) 14510–14521.
- [29] T. Ressler, WinXAS: A Program for X-ray Absorption Spectroscopy Data Analysis under MS-Windows, *J. Synchrotron Radiat.* 5 (1998) 118–122.
- [30] A. Ankudinov, B. Ravel, J. Rehr, S. Conradson, Real-space multiple-scattering calculation and interpretation of x-ray-absorption near-edge structure, *Phys. Rev. B* 58 (1998) 7565.
- [31] F. Lou, M.E.M. Buan, N. Muthuswamy, J.C. Walmsley, M. Rønning, D. Chen, One-step electrochemical synthesis of tunable nitrogen-doped graphene, *J. Mater. Chem. A* 4 (2016) 1233–1243.
- [32] H.A. Gasteiger, S.S. Kocha, B. Sompalli, F.T. Wagner, Activity benchmarks and requirements for Pt, Pt-alloy, and non-Pt oxygen reduction catalysts for PEMFCs, *Appl. Catal. B* 56 (2005) 9–35.
- [33] U.I. Koslowski, I. Abs-Wurmbach, S. Fiechter, P. Bogdanoff, Nature of the catalytic centers of porphyrin-based electrocatalysts for the ORR: a correlation of kinetic current density with the site density of Fe-N₄ centers, *J. Phys. Chem. C* 112 (2008) 15356–15366.
- [34] Z.F. Huang, J. Wang, Y. Peng, C.Y. Jung, A. Fisher, X. Wang, Design of efficient bifunctional oxygen reduction/evolution electrocatalyst: recent advances and

perspectives, *Adv. Energy Mater.* 7 (2017) 1700544.

[35] R. Lang, W. Xi, J.C. Liu, Y.T. Cui, T. Li, A.F. Lee, F. Chen, Y. Chen, L. Li, L. Li, J. Lin, S. Miao, X. Liu, A.Q. Wang, X. Wang, J. Luo, B. Qiao, J. Li, T. Zhang, Non defect-stabilized thermally stable single-atom catalyst, *Nat. Commun.* 10 (2019) 234.

[36] L. Zhang, L. Han, H. Liu, X. Liu, J. Luo, Potential-cycling synthesis of single platinum atoms for efficient hydrogen evolution in neutral media, *Angew. Chem. Int. Ed.* 56 (2017) 13694–13698.

[37] Y. Chen, S. Ji, Y. Wang, J. Dong, W. Chen, Z. Li, R. Shen, L. Zheng, Z. Zhuang, D. Wang, Y. Li, isolated single iron atoms anchored on n-doped porous carbon as an efficient electrocatalyst for the oxygen reduction reaction, *Angew. Chem. Int. Ed.* 56 (2017) 6937–6941.

[38] C. Zhu, Q. Shi, B.Z. Xu, S. Fu, G. Wan, C. Yang, S. Yao, J. Song, H. Zhou, D. Du, S.P. Beckman, D. Su, Y. Lin, Hierarchically porous M–N–C (M = Co and Fe) single-atom electrocatalysts with robust MN_x active moieties enable enhanced ORR performance, *Adv. Energy Mater.* 8 (2018) 1801956.

[39] R. Zhang, C. Zhang, W. Chen, FeP embedded in N, P dual-doped porous carbon nanosheets: an efficient and durable bifunctional catalyst for oxygen reduction and evolution reactions, *J. Mater. Chem. A* 4 (2016) 18723–18729.

[40] K. Chen, X. Huang, C. Wan, H. Liu, Hybrids based on transition metal phosphide (Mn₂P, Co₂P, Ni₂P) nanoparticles and heteroatom-doped carbon nanotubes for efficient oxygen reduction reaction, *RSC Adv.* 5 (2015) 92893–92898.

[41] Y. Hu, J.O. Jensen, W. Zhang, L.N. Cleemann, W. Xing, N.J. Bjerrum, Q. Li, Hollow spheres of iron carbide nanoparticles encased in graphitic layers as oxygen reduction catalysts, *Angew. Chem. Int. Ed.* 53 (2014) 3675–3679.

[42] M. Xiao, J. Zhu, L. Feng, C. Liu, W. Xing, Meso/macroporous nitrogen-doped carbon architectures with iron carbide encapsulated in graphitic layers as an efficient and robust catalyst for the oxygen reduction reaction in both acidic and alkaline solutions, *Adv. Mater.* 27 (2015) 2521–2527.

[43] H. Jiang, Y. Zhu, Q. Feng, Y. Su, X. Yang, C. Li, Nitrogen and phosphorus dual-doped hierarchical porous carbon foams as efficient metal-free electrocatalysts for oxygen reduction reactions, *Chemistry* 20 (2014) 3106–3112.

[44] D.S. Yang, D. Bhattacharjya, S. Inamdar, J. Park, J.S. Yu, Phosphorus-doped ordered mesoporous carbons with different lengths as efficient metal-free electrocatalysts for oxygen reduction reaction in alkaline media, *J. Am. Chem. Soc.* 134 (2012) 16127–16130.

[45] M. Li, T. Liu, X. Bo, M. Zhou, L. Guo, S. Guo, Hybrid carbon nanowire networks with Fe-P bond active site for efficient oxygen/hydrogen-based electrocatalysis, *Nano Energy* 33 (2017) 221–228.

[46] E. Gil, J. Cortés, I. Iturrriza, N. Ordás, XPS and SEM analysis of the surface of gas atomized powder precursor of ODS ferritic steels obtained through the STARS route, *Appl. Surf. Sci.* 427 (2018) 182–191.

[47] G.K. Reddy, P. Boolchand, P.G. Smirniotis, Unexpected behavior of copper in modified ferrites during high temperature WGS reaction-aspects of Fe³⁺↔Fe²⁺ redox chemistry from Mössbauer and XPS studies, *J. Phys. Chem. C* 116 (2012) 11019–11031.

[48] Y. Peng, Z. Li, D. Xia, L. Zheng, Y. Liao, K. Li, X. Zuo, Probing the influence of the center atom coordination structure in iron phthalocyanine multi-walled carbon nanotube-based oxygen reduction reaction catalysts by X-ray absorption fine structure spectroscopy, *J. Power Sources* 291 (2015) 20–28.

[49] J. Yang, D.J. Liu, N.N. Kariuki, L.X. Chen, Aligned carbon nanotubes with built-in FeN₄ active sites for electrocatalytic reduction of oxygen, *Chem. Commun.* 36 (2008) 329–331.

[50] U.I. Kramm, I. Herrmann-Geppert, J. Behrends, K. Lips, S. Fiechter, P. Bogdanoff, On an easy way to prepare metal–nitrogen doped carbon with exclusive presence of MeN₄-type sites active for the ORR, *J. Am. Chem. Soc.* 138 (2016) 635–640.

[51] Y. Li, B. Hulyageqi, W. Haschaolu, Z. Song, O. Tegus, I. Nakai, EXAFS study of Mn_{1.28}Fe_{0.67}P_{0.46}Si_{0.54} compound with first-order phase transition, *J. Electron Spectrosc. Relat. Phenom.* 196 (2014) 104–109.

[52] H. Demirkiran, Y. Hu, L. Zuin, N. Appathurai, P.B. Aswath, XANES analysis of calcium and sodium phosphates and silicates and hydroxyapatite-Bioglass® 45S5 co-sintered bioceramics, *Mater. Sci. Eng. C* 31 (2011) 134–143.

[53] Y. Lin, L. Yang, Y. Zhang, H. Jiang, Z. Xiao, C. Wu, G. Zhang, J. Jiang, L. Song, Defective Carbon-CoP Nanoparticles Hybrids with Interfacial Charges Polarization for Efficient Bifunctional Oxygen Electrocatalysis, *Adv. Energy Mater.* (2018) 1703623.

[54] J. Kruse, P. Leinweber, K.U. Eckhardt, F. Godlinski, Y. Hu, L. Zuin, Phosphorus L_{2,3}-edge XANES: overview of reference compounds, *J. Synchrotron Radiat.* 16 (2009) 247–259.

[55] S. Yang, D. Wang, G. Liang, Y.M. Yiu, J. Wang, L. Liu, X. Sun, T.K. Sham, Soft X-ray XANES studies of various phases related to LiFePO₄ based cathode materials, *Energy Environ. Sci.* 5 (2012) 7007–7016.

[56] X. Lv, K. Nie, H. Lan, X. Li, Y. Li, X. Sun, J. Zhong, S.T. Lee, Fe₂TiO₅-incorporated hematite with surface P-modification for high-efficiency solar water splitting, *Nano Energy* 32 (2017) 526–532.

[57] H.B. Yang, J. Miao, S.F. Hung, J. Chen, H.B. Tao, X. Wang, L. Zhang, R. Chen, J. Gao, H.M. Chen, Identification of catalytic sites for oxygen reduction and oxygen evolution in N-doped graphene materials: development of highly efficient metal-free bifunctional electrocatalyst, *Sci. Adv.* 2 (2016) e1501122.

[58] P. Chen, T. Zhou, L. Xing, K. Xu, Y. Tong, H. Xie, L. Zhang, W. Yan, W. Chu, C. Wu, Atomically dispersed iron–nitrogen species as electrocatalysts for bifunctional oxygen evolution and reduction reactions, *Angew. Chem. Int. Ed.* 56 (2017) 610–614.

[59] G.L. Chai, K. Qiu, M. Qiao, M.M. Titirici, C. Shang, Z. Guo, Active sites engineering leads to exceptional ORR and OER bifunctionality in P, N Co-doped graphene frameworks, *Energy Environ. Sci.* 10 (2017) 1186–1195.

[60] M. Li, L. Zhang, Q. Xu, J. Niu, Z. Xia, N-doped graphene as catalysts for oxygen reduction and oxygen evolution reactions: theoretical considerations, *J. Catal.* 314 (2014) 66–72.

[61] L.C. Chin, Y.H. Yi, W.C. Chang, H.Y. Tuan, Significantly improved performance of red phosphorus sodium-ion anodes with the addition of iron, *Electrochim. Acta* (2017) 266.

[62] X. Chen, L. Yu, S. Wang, D. Deng, X. Bao, Highly active and stable single iron site confined in graphene nanosheets for oxygen reduction reaction, *Nano Energy* 32 (2017) 353–358.

[63] J.K. Nørskov, J. Rossmeisl, A. Logadottir, L. Lindqvist, J.R. Kitchin, T. Bligaard, H. Jonsson, Origin of the overpotential for oxygen reduction at a fuel-cell cathode, *J. Phys. Chem. B* 108 (2004) 17886–17892.

[64] V. Tripković, E. Skúlasdóttir, S. Siahrostami, J.K. Nørskov, J. Rossmeisl, The oxygen reduction reaction mechanism on Pt (1 1 1) from density functional theory calculations, *Electrochim. Acta* 55 (2010) 7975–7981.

[65] A.U. Nilekar, M. Mavrikakis, Improved oxygen reduction reactivity of platinum monolayers on transition metal surfaces, *Surf. Sci.* 602 (2008) L89–L94.

[66] J.K. Nørskov, T. Bligaard, J. Rossmeisl, C.H. Christensen, Towards the computational design of solid catalysts, *Nat. Chem.* 1 (2009) 37.